TU Delft

Delft University of Technology

3D Printing of Flow-Inspired Anisotropic Patterns with Liquid Crystalline Polymers

Houriet, Caroline; Damodaran, Vinay; Mascolo, Chiara; Gantenbein, Silvan; Peeters, Daniël; Masania, Kunal

DOI
10.1002/adma.202307444

Publication date
2023

Document Version
Final published version

Published in
Advanced Materials

Citation (APA)
Houriet, C., Damodaran, V., Mascolo, C., Gantenbein, S., Peeters, D., & Masania, K. (2023). 3D Printing of Flow-Inspired Anisotropic Patterns with Liquid Crystalline Polymers. *Advanced Materials*, *36*(11), Article 2307444. https://doi.org/10.1002/adma.202307444

Important note
To cite this publication, please use the final published version (if applicable).
Please check the document version above.

Copyright
Other than for strictly personal use, it is not permitted to download, forward or distribute the text or part of it, without the consent of the author(s) and/or copyright holder(s), unless the work is under an open content license such as Creative Commons.

Takedown policy
Please contact us and provide details if you believe this document breaches copyrights.
We will remove access to the work immediately and investigate your claim.

This work is downloaded from Delft University of Technology.
For technical reasons the number of authors shown on this cover page is limited to a maximum of 10.

Check for updates

ADVANCED MATERIALS
www.advmat.de

3D Printing of Flow-Inspired Anisotropic Patterns with Liquid Crystalline Polymers

*Caroline Houriet, Vinay Damodaran, Chiara Mascolo, Silvan Gantenbein, Daniël Peeters, and Kunal Masania**

Anisotropic materials formed by living organisms possess remarkable mechanical properties due to their intricate microstructure and directional freedom. In contrast, human-made materials face challenges in achieving similar levels of directionality due to material and manufacturability constraints. To overcome these limitations, an approach using 3D printing of self-assembling thermotropic liquid crystal polymers (LCPs) is presented. Their high stiffness and strength is granted by nematic domains aligning during the extrusion process. Here, a remarkably wide range of Young's modulus from 3 to 40 GPa is obtained by utilizing directionality of the nematic flow the printing process. By determining a relationship between stiffness, nozzle diameter, and line width, a design space where shaping and mechanical performance can be combined is identified. The ability to print LCPs with on-the-fly width changes to accommodate arbitrary spatially varying directions is demonstrated. This unlocks the possibility to manufacture exquisite patterns inspired by fluid dynamics with steep curvature variations. Utilizing the synergy between this path-planning method and LCPs, functional objects with stiffness and curvature gradients can be 3D-printed, offering potential applications in lightweight sustainable structures embedding crack-mitigation strategies. This method also opens avenues for studying and replicating intricate patterns observed in nature, such as wood or turbulent flow using 3D printing.

1. Introduction

Anisotropic materials can be formed by living organisms such as the cellulose fibers in wood grains[1] and fiber bundles in osteons of bone.[2] Their microstructures are shaped with spatially tunable stiffness gradients and sharp orientation changes[3] in order to accommodate stresses and morphogenesis of the living organism in an efficient manner.[4] This freedom enables remarkable mechanical properties while keeping energy consumption low and using weak building blocks.[5] In contrast, despite the larger processing energy and stronger base materials used, human-made materials such as composites cannot be shaped with similar levels of anisotropy and directionality freedom.[6] While the latter can be achieved with 3D printing such as fused filament fabrication (FFF), or via automated composite tape laying,[7] compatible anisotropic materials are typically fiber-filled.[8] Paradoxically, these fibers restrict directional freedom due to their intrinsic stiffness and relatively large size. Problems such as wrinkling or fiber breakage have been reported[9] and often result in the need to predetermine curvature constraints in the design space.[6]

To remove these constraints, one could shape polymer chains that self-assemble into ordered liquid crystalline domains in the melt.[10] In liquid crystal polymers (LCPs), the direction of the molecules in each domain was found to align with the direction of extrusion by the nozzle of the FFF 3D printer.[10] Because alignment is strongly influenced by elongational flow, melt-spun LCP fibers with remarkably high mechanical performance were spun and integrated into recyclable and strong all-fiber lightweight materials.[11] Despite attaining high properties in printed objects, the need for the LCP fibers to undergo stretching has limited their integration to unidirectional straight-line patterns. Reconciling these properties in tailored printed objects that closely resemble the exquisite microstructure of natural materials remains a challenge.

To achieve this goal, the printed lines should follow a spatially varying directional field while avoiding gaps or overlaps. One way to enable manufacturing could be to allow line width to vary by changing extrusion rate.[12–14] However, increasing the line width negatively affects the stiffness[15] and failure mode[16] of polymers because of a loss of alignment.[17,18] As a result, the

C. Houriet, V. Damodaran, K. Masania
Shaping Matter Lab
Faculty of Aerospace Engineering
Delft University of Technology
Kluyverweg 1, Delft 2629 HS, Netherlands
E-mail: k.masania@tudelft.nl

C. Mascolo[+], S. Gantenbein[+], K. Masania
Complex Materials
Department of Materials
ETH Zürich, Zürich 8093, Switzerland

D. Peeters
Faculty of Aerospace Engineering
Delft University of Technology
Kluyverweg 1, Delft 2629 HS, Netherlands

The ORCID identification number(s) for the author(s) of this article can be found under https://doi.org/10.1002/adma.202307444

[+]Present address: NematX AG, Förrlibuckstrasse 150, Zürich 8005, Switzerland

© 2023 The Authors. Advanced Materials published by Wiley-VCH GmbH. This is an open access article under the terms of the Creative Commons Attribution-NonCommercial License, which permits use, distribution and reproduction in any medium, provided the original work is properly cited and is not used for commercial purposes.

DOI: 10.1002/adma.202307444

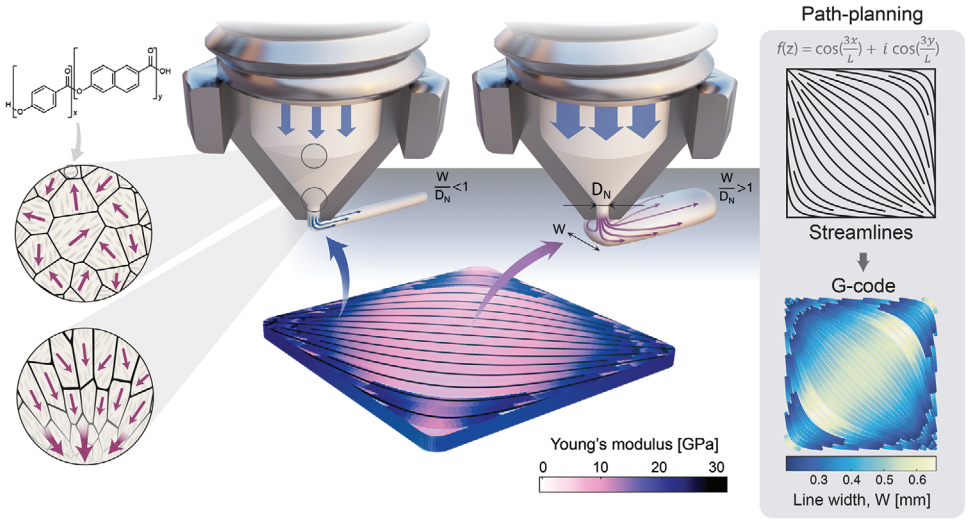

Figure 1. Overview of the printing of liquid crystal polymer patterns with line width variation. The nematic domains of an aromatic co-polyester are subjected to shear and extensional flow during extrusion via the 3D-printer nozzle, which promotes their homogeneous alignment. By varying the extrusion rate, the flow behavior upon exit can be controlled. The distribution of nematic domains remains parallel to the travel (longitudinal) direction when the ratio of line width W to nozzle diameter D_N is below unity. In contrast, above unity, a transverse component of the flow leads a portion of the domains to solidify at an angle to the longitudinal direction. A controlled gradient of stiffness can be printed within one line by varying line width. The axial stiffness of each print path can be predicted from line width and printing nozzle diameter by utilizing a scaling law. A path-planning algorithm mindful of user-input line width bounds allows to generate complex patterns that make use of this feature.

path-planning method should carefully control the spacing between printed lines to balance manufacturability and desired performance.

We hypothesize that streamlines, which are commonly used in fluid mechanics to visualize flow, could accurately generate toolpaths describing complex 3D-printed microstructures with LCP. The characteristic of this approach, beyond its mathematical elegance, is to produce multiple smooth individual paths instead of one tortuous cyclic path that is generally shown for single continuous motion approaches.[19–25] Recently, evenly distributed streamlines[26] were generated for printed paths of fixed width following principal stress directions. Studies using streamlines have mainly focused on computing toolpath location for fibers flowing around a hole based on the potential flow functions describing flow around a cylinder,[27–29] akin to the microstructure of wood around a knot.

To fully exploit the unusual combination of anisotropy and directionality freedom of LCP, we extend the streamline approach to path-planning for 3D printing aiming for dense filling of any pattern. By ensuring a distribution of streamlines such that all gaps can effectively be filled by the flowing material, we show that the LCPs can be 3D-printed into complex shapes with steep curvature variations by tuning the width of a line during the printing process. To explore the potential of such curvature changes, we generate angle fields via analytical functions traditionally describing potential flows in fluid dynamics. This enables us to easily superimpose local and global flow features. This path-planning approach combined with the anisotropy and directionality freedom of LCP, allows for the first time to manufacture patterns such as vortices with FFF, showing significant mechanical benefits.

2. Results and Discussion

2.1. Printing Strategy

To combine high anisotropy with full directionality freedom, a thermotropic liquid crystal polymer displaying a self-aligning behavior is deposited via extrusion 3D printing.[10,11,30] In the melt at rest, the polydomain structure of the aromatic co-polyester shown in **Figure 1** is macroscopically unoriented, while the liquid crystalline orientational order is preserved within the nematic domains.[31] Above its melting point, its rigid molecular segments self-assemble into nematic domains of a few micrometers in size.[32] Anisotropy is generated in the melt by shear and extensional flow arising during extrusion through the converging nozzle of the 3D printer. As the polymer exits the nozzle and is exposed to ambient temperature, rapid cooling enables the co-polymer to solidify and preserve alignment before the nematic order can relax into its macroscopically unoriented configuration.[10] When a print line is deposited by the moving nozzle onto the heated bed with a fixed height $h = 100\,\mu m$, changing the amount of material pushed into the nozzle results in a proportional change in the line width W, due to the conservation of volume. When the ratio between line width W and nozzle diameter D_N is close to or below unity, the flow orientation aligns with the nozzle travel direction.[33] However, when the volumetric flow rate is increased, the polymer chains may partially adopt a transverse component. The line width change causing a gradient of stiffness represents a remarkably simple method to modulate the mechanical performance due to the capability of producing both stiff-strong and soft-ductile lines, with an order of magnitude difference in the stiffness, from a single material system. The low viscosity of the polymer enables us to utilize this line

© 2023 The Authors. Advanced Materials published by Wiley-VCH GmbH

15214095, 0, Downloaded from https://onlinelibrary.wiley.com/doi/10.1002/adma.202307444 by Tu Delft, Wiley Online Library on [11/01/2024]. See the Terms and Conditions (https://onlinelibrary.wiley.com/terms-and-conditions) on Wiley Online Library for rules of use; OA articles are governed by the applicable Creative Commons License

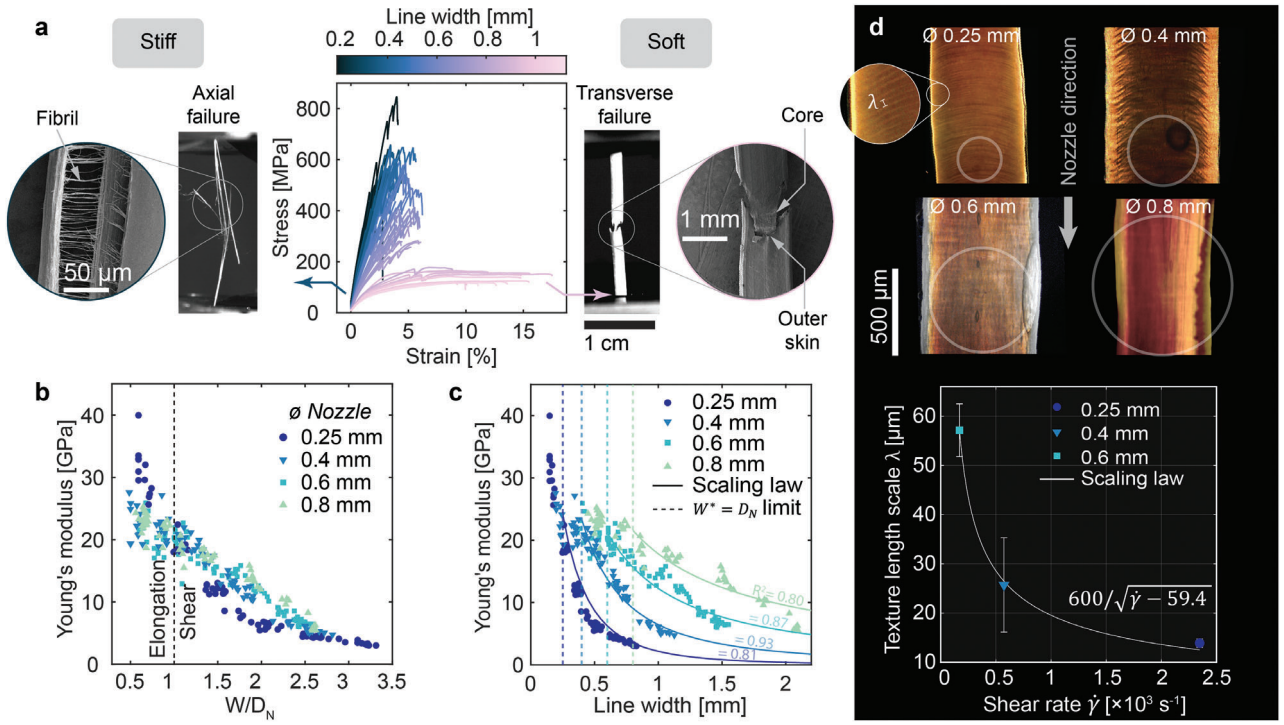

Figure 2. Line width influences the microstructure and mechanical response of the 3D-printed liquid crystal polymer. A) The tensile behavior of printed lines transitions from brittle to ductile with increasing line width due to increasing transverse flow from the nozzle. In the stiff samples, a fibrillar failure is identified in SEM while in the softer samples, a skin and core structure is observed. B) Increasing the ratio of printed line width W to nozzle diameter D_N leads to a decrease in Young's modulus for the four different nozzle diameters that were tested. C) The Young's modulus scales with line width by a power law of exponent $-\frac{\pi}{4D_N}$ beyond a threshold where shear flow dominates over elongational flow. D) Transmitted-light darkfield microscopy of constant line width samples printed with four different nozzle diameters demonstrate texturing. Shear bands, typical of aligned nematic polymers, decrease in intensity with increasing nozzle diameter and decreasing shear rate. Their wavelength follows a reciprocal square-root shear scaling.

width variation to create fully dense parts with large curvature changes. Once the angle fields describing a pattern have been generated, the path planning algorithm generates corresponding streamlines as toolpath, such that each streamline is placed at a fillable distance to its neighbors.

2.2. Dependence of Extruded Line Width on Mechanical Properties

The influence of varying line width on the tensile and microstructural properties of single printed lines of LCP was investigated. The layer height h, print temperature T_{print} and speed V_{print} were kept constant at 0.1 mm, 330 °C and 60 mm s^{-1} respectively. The volumetric flow rate was calculated as $Q = V_{print}\, hW$ where W is the target line width. Printed lines were tested in tension. For a single nozzle diameter D_N of 0.4 mm, stress–strain curves in **Figure 2a** show a notable change in failure behavior from brittle to ductile with increasing line width. Imaging of the specimen after failure reveals that either behavior is also linked to significant differences in the micro- and macroscopic morphologies.

The lines printed with a width smaller than the nozzle diameter (0.4 mm) demonstrated a high mechanical performance. For the best-performing sample, we obtained a modulus of 27.6 GPa and an ultimate tensile strength of 847 MPa corresponding to a 4% failure strain. The fibers were found to fail in a quasi-brittle manner. Such a failure behavior has been widely documented for highly aligned LCPs such as melt-spun or extruded filaments with high draw ratios displaying a fibrillar structure.[33,34] Scanning electron microscopy (SEM) revealed a typical fibrillar microstructure in our samples as well, with fibrils of ≈0.1 µm bridging broken ends. The axial cracks indicate that the polymer chains are so highly aligned that a shear fracture is more likely to take place. The chain modulus of the LCP is reported much larger at 122 GPa than the molecular shear modulus of 1.7 GPa. The weak van der Waals forces holding together the oriented fibrils of LCP explain the prevalence of chain slippage over chain stretching.[33] In hardwoods and softwoods loaded in tension parallel to the grain, a similar slippage between microfibrils occurs and creates a fibrillar fracture surface with an unraveling of the S2 layer from the S1 layer.[35] Moreover, the toughening mechanism of wood involves microfibril ligaments bridging the crack and crack-tip blunting.[36] In our case, the presence of these fibrils effectively allows the printed lines to stay connected after fracture. In contrast, the specimens printed with line widths larger than the nozzle diameter show a ductile fracture, with a skin/core behavior.[10] The stiffer skin fails first while the more compliant core remains embedded, revealing a conical fracture surface shown in the SEM image. We obtained a modulus of 4.7 GPa and a strength of 115 MPa corresponding to a 10% failure strain for the specimen with the largest line width.

© 2023 The Authors. Advanced Materials published by Wiley-VCH GmbH

15214095, 0, Downloaded from https://onlinelibrary.wiley.com/doi/10.1002/adma.202307444 by Tu Delft, Wiley Online Library on [11/01/2024]. See the Terms and Conditions (https://onlinelibrary.wiley.com/terms-and-conditions) on Wiley Online Library for rules of use; OA articles are governed by the applicable Creative Commons License

To further elucidate the effect of nozzle diameter, measurements of the tensile response were conducted for four nozzle diameters and different values of $\frac{W}{D_N}$ as shown in Figure 2b,c. The elastic modulus was observed to vary widely with $\frac{W}{D_N}$ for all nozzle sizes that were studied, both for single lines and unidirectional tensile samples, shown in Figure S3 (Supporting Information). For example, the 0.25 mm nozzle shows the widest property variation, Young's modulus ranges from 3 GPa for the widest lines to 40 GPa for the thinnest lines. The strength variation also covers one order of magnitude up to a value of 1.28 GPa (Figure S1a, Supporting Information). A decrease in mechanical properties with increasing linewidth was reported in the work of Yan et al.[15] for CF-PLA, CF-ABS and CF-PA. However, the span of this variation was far narrower, with Young's moduli ranging from 2.8 to 4.2 GPa for respective line widths between 0.48 and 0.72 mm, as shown in Figure S2 (Supporting Information). This has been associated with a wider distribution of fiber orientations with increasing widths of short-fiber composites.[15] A transverse flow component was identified using numerical simulations of the 3D flow during extrusion.[17,18] For narrow extruded lines, fibers are reportedly aligned in the flow direction, while wider extrusion causes the polymer melt to flow partially in the transverse direction, leading to a larger distribution of angles for the anisotropic fillers in the melt.[15] We hypothesize the same behavior where a larger flow rate induces a perpendicular component into the motion of the fluid, which in turn causes loss of alignment in our LCP samples. In order to shed light on this behavior, the threshold line width beyond which transverse flow occurs can be investigated. Considering a case where transverse flow, that is, flow in the y-direction, is absent, the exiting material can only increase the height of the print line through bulging. In this case, the volume conservation equation simplifies to 2D along planes normal to y. In other words, all cross-sectional areas of the melt pool and printed line along the transverse dimension y should be at equilibrium. Using plug flow assumption inside the nozzle allows us to define the velocity V_N of the melt inside the nozzle before exit as a constant. During one second, a cylindrical volume of height V_N and diameter D_N is extruded. The sectional area of this cylinder along y is $A_{in} = D_{chord}(y) \times V_N$ where $D_{chord}(y) = \sqrt{\left(\frac{D_N}{2}\right)^2 - y^2}$. Steady exit of the polymer implies that A_{in} should equal $A_{out} = h \times V_{line}(y)$, the area of the printed line deposited without bulging. Consequently, the length deposited per second $V_{line}(y) = \frac{V_N}{h}\sqrt{\left(\frac{D_N}{2}\right)^2 - y^2}$ is only defined within the bounds $y = \pm\frac{D_N}{2}$. The value $W = D_N$ plotted in Figure 2c may therefore be considered as a threshold W^* above which transverse flow should occur. Figure 2c further indicates that the relationship between elastic modulus and line width follows a trend shifting from linear to power-law with decreasing nozzle diameter. A scaling law was developed using Buckingham's theorem of dimensional analysis[37] with the independent variables D_N and W. For measurements above W^*, the scaling law $E = E_o \frac{D_N}{L_o}\left(\frac{W}{L_o} + \frac{h}{D_N}\right)^{-\frac{\pi L_0}{4D_N}}$ where $E_0 = 25$ GPa, and $L_0 = 1$ mm, describes the experimental data for the four nozzle diameters that were studied, with R^2 values ranging from 0.80 to 0.93 demonstrating a good correlation. For all nozzle diameters except 0.25 mm, the data depart from the fitting trend below this value. We hypothesize that elongational flow at low flow rates causes pressure inhomogeneities, which translate into geometrically inconsistent filaments for mechanical testing. The scatter thus becomes higher, in particular for the strength values. In contrast, for the 0.25 mm nozzle, the aspect ratio of the filament is closer to 1 for the thinnest lines ($h = 0.1$ mm, $W = 0.17$ mm), therefore the extruded melt needs to undergo less strain to fit the expected cross-section. This may facilitate the production of consistent diameters even under extensional flow. As such, the scaling law can be used as a non-linear relationship to predict stiffness from line width beyond the threshold at which transverse flow occurs.

To further understand the influence of transverse flow on mechanical properties, flow behavior can also be conceptually split between elongational flow and shear flow. These two flows coexist during 3D printing since the nozzle is a die geometry with a contraction cone promoting elongational flow, and a straight channel promoting shear flow. Elongational flow is known to be more effective than shear flow in causing molecular orientation in LCPs,[38] even more so than other polymers due to the cooperative nature of the molecules in the nematic threshold of line width W^* where no transverse flow occurs. The apparent shear rate $\dot{\gamma}$ in the nozzle is computed with the relationship $\dot{\gamma} = \frac{32\,Q}{\pi(D_N)^3}$. The shear rate imposed at the 0.25 mm diameter nozzle tip spans two orders of magnitude, from 50 to 3500 s^{-1} for line width ranging from 0.15 to 0.82 mm. With such a range in the shear rate, the melting behavior can be very different in terms of viscosity, texture, and rheology.[32] The largest apparent shear rate is observed for the most compliant specimens, with Young's modulus of 3 GPa. In Figure S1b (Supporting Information), Young's modulus is plotted against the shear rate for different nozzle diameters. Single lines printed with different nozzle diameters at the same shear rate yield vastly different Young's moduli. These elements indicate that shear inside the nozzle alone cannot explain the discrepancy in alignment. A closer look into the microscopic orientation within the printed lines is needed.

In Figure 2d, four lines of width ranging between 0.5 and 0.6 mm were printed with different nozzle diameters. The lines were polished down to 20–40 µm thickness and imaged with crossed-polarized transmitted light microscopy. A banded texture of horizontal streaks can be observed, whose wavelength λ increases with nozzle diameter until it becomes virtually indistinguishable at $D_N = 0.8$ mm. Such a phenomenon is commonly reported after cessation of shear for a wide range of LCPs, including the thermotropic LCP studied here.[32,39,40] Their formation has been linked to elastic energy stored in the nematic texture during flow, which is released through the unwinding of the nematic directors upon flow cessation.[32] This induces a formation of periodic extinctions observable with transmitted light microscopy under crossed-polarizers.[41,42] The bands can be characterized by their wavelength, which varies with the shear conditions. For $D_N = 0.8$ mm where the banded texture cannot be clearly distinguished, the threshold between elongation and sideway flow W^* is above the line width $W = 0.55$ mm of this specimen. At this line width, the shear rate $\dot{\gamma}$ =65 s^{-1} is lowest, and the strong elongational flow imposed at the exit of the nozzle will predominate over existing textures caused by low shear and facilitate molecular re-alignment. To further confirm the nature of

© 2023 The Authors. Advanced Materials published by Wiley-VCH GmbH

15214095, 0, Downloaded from https://onlinelibrary.wiley.com/doi/10.1002/adma.202307444 by Tu Delft, Wiley Online Library on [11/01/2024]. See the Terms and Conditions (https://onlinelibrary.wiley.com/terms-and-conditions) on Wiley Online Library for rules of use; OA articles are governed by the applicable Creative Commons License

these bands, we relate the wavelength of the three visible textures to a texture length-scale ℓ_t, for which extensive theoretical work was conducted. Previous research[43,44] has demonstrated that in a flow region where the Deborah number *De* is below unity, the texture of sheared, flow-aligning rigid rod LCP can be related to shear by the following relation $\ell_t \propto \frac{1}{\sqrt{\dot{\gamma} - a}}$. The agreement between the observed wavelength and this scaling law confirms that these bands are indeed shear bands.

As is the case for the three printed lines with visible textures, the presence of a banded texture has been reported to play a detrimental role in the stiffness along flow direction,[45] because the recoil of the nematic directors causes a spatial periodicity of the molecular orientation.[41] At nozzle diameters of 0.25 and 0.4 mm, the banded texture is not a straight line but a curve with an angle of ≈30° on the edges. Such curved banded structures have also been reported for thin sections of injection molded specimens of other thermotropic LCPs,[46] where it is suggested that the banded structure runs perpendicular to the flow. In such a case, these curved banded structures are a strong indication of transverse flow behavior.

The strong dependency of line width upon tensile properties for 3D-printed single lines of LCP is caused by the opposing behaviors of transverse flow and extensional flow during the deposition of the melt. Compared to approaches that promote anisotropic re-arrangement during printing using, for example, nozzle rotation,[47,48] this method relies on nematic self-assembly of the polymer under the different processing pressures to change its resulting stiffness. The myriad of routes explored to create stiffness gradients, such as porosity gradients[14,25] or compositional gradients,[49,50] and their omnipresence in the natural world are indicators of how promising they may be to engineering, should there be an easy approach to manufacture them.[8] For instance, tailoring such stiffness gradients allows the development of single-material bio-inspired crack-arresters similar to those obtained by alternating stiff and soft polymeric layers.[51] The explored range of stiffness in our work opens new paths for tuning compliance and deformation before failure on the fly, simply by changing the processing conditions of the polymer.

2.3. Distance-Aware Generation of Flow-Inspired Patterns

As illustrated in Figure 2, the anisotropy granted by LCP as well as the wide range of line widths that can be extruded, allow the realization of complex infill patterns. However, typical slicing approaches tend to assign a fixed line width for each printing feature, such as perimeters or infills, and fill volumes with a fixed geometrical repeat pattern, like gyroid or rectilinear. A versatile method allowing both a freeform distribution of angles and a fully dense coverage of the shape by print paths is therefore needed.

Two main steps are followed to generate streamlines which will form the print paths. The first step involves crafting an angle field corresponding to the target pattern. In the second step, the streamlines are located such that the maximum distance between neighbors does not exceed constraints of manufacturability or desired mechanical behavior. These streamlines are then processed to create manufacturable patterns.

The angle field corresponding to the target pattern can be considered as user input to the streamline generation algorithm. Inspired by fluid dynamics, we propose a facile way of generating patterns by using mathematical functions in the complex domain. We make use of a transformation of the vector space $\mathbb{R}^2$ representing the 2D rectangular design domain into the complex field $\mathbb{C}$. For any given point (x, y) in the domain, we introduce the complex scalar $z = x + iy$. Any complex differentiable function $f : \mathbb{C} \mapsto \mathbb{C}$ can then transform the 2D real space into a complex scalar field. At $z = z_o = x_o + i\,y_o$, the argument of complex number $f(z_0)$ determines the direction followed by a streamline at (x_o, y_o). In fluid dynamics, such a transformation is performed from a real domain to the complex plane to obtain analytical solutions for an irrotational incompressible flow. The scalar function f then represents a complex speed, defined as $f(z) = \frac{dp}{dz} = u - iv$. The complex potential function p is defined as $p(x, y) = \Phi(x, y) + i\psi(x, y)$, where ψ is the stream function and Φ is the velocity potential of an incompressible fluid satisfying Cauchy–Riemann equations.[52] The vertical and horizontal components of the speed (u, v) are by definition $u = \frac{\partial \Phi}{\partial x}$ and $v = \frac{\partial \Phi}{\partial y}$. With knowledge of f(z), the real velocity components (u, v) can be found with $(\mathrm{Re}(f), -\mathrm{Im}(f))$. It is worth noting that here, any complex differentiable function may generate a pattern, regardless whether it represents a physical flow. Three exemplary patterns generated by elementary potential flows are illustrated in **Figure 3a** along with the corresponding complex velocities[52]: a point source, a vortex, and a right-angle flow. More complex flow fields such as flows through an opening or normal to a flat plate, can also be described analytically with this method,[53] and may also be further explored to create relevant patterns for solid mechanics.

After a velocity field has been created, streamlines can be generated. They are defined as a family of curves whose tangent vectors constitute the velocity vector field of the flow. In this work, streamlines are generated to become tool paths for the printer to follow. To achieve this, the algorithm of Mebarki[54] is implemented and adapted such that lines are spaced by manufacturable widths, as illustrated in Figure S6 (Supporting Information). At each calculation step, at the location where the largest circle can be fit between two streamlines, a new streamline is inserted until the largest circle that can be fit is smaller than W_{upper}, the largest desired line width. The new streamline is immediately trimmed if it becomes spaced to its neighbors by a distance smaller than W_{lower}, the lowest desired or manufacturable line width. Distances between lines are then extracted to obtain the extrusion amount necessary for each segment of the toolpath. The resulting distribution of line width shown in Figure 3b indicates the successful replication of the mathematical flow fields. After the streamlines have been generated, simplified, sorted, and transformed into g-code format, they can be 3D-printed, as illustrated for the three elementary flow fields in Figure 3c.

To quantitatively assess the ability of the printing method to produce a freeform infill, the image of the printed object in Figure 3c is compared to the planned toolpath. Curves that are orthogonal to the planned toolpaths are generated to intersect between 500 and 600 printed paths. Along these intersections, the planned line width is compared to the distance between black pixels in the image. Figure S6 (Supporting Information) shows

© 2023 The Authors. Advanced Materials published by Wiley-VCH GmbH

15214095, 0, Downloaded from https://onlinelibrary.wiley.com/doi/10.1002/adma.202307444 by Tu Delft, Wiley Online Library on [11/01/2024]. See the Terms and Conditions (https://onlinelibrary.wiley.com/terms-and-conditions) on Wiley Online Library for rules of use; OA articles are governed by the applicable Creative Commons License

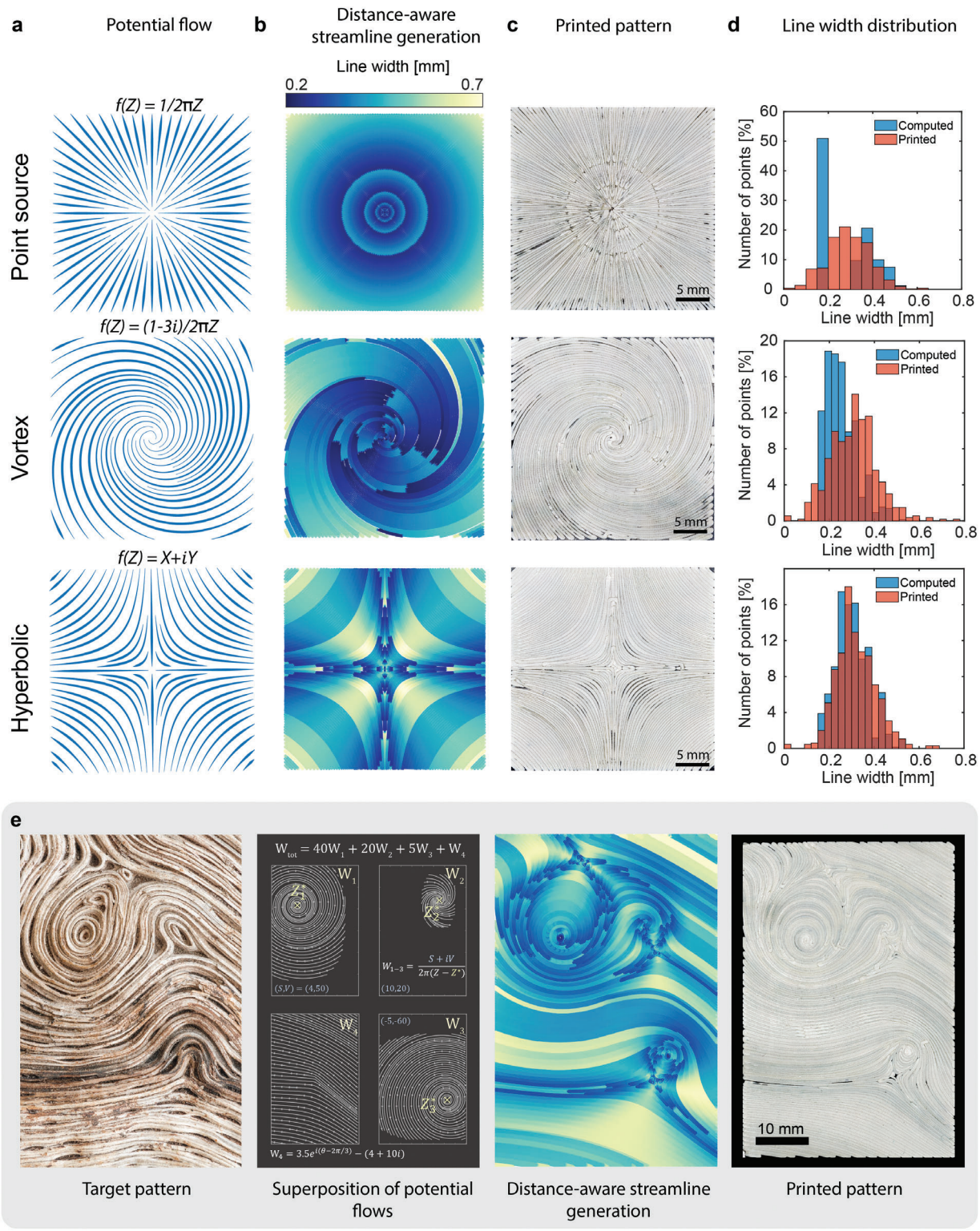

Figure 3. Complex printable patterns are generated via the superposition of elementary potential flows. A) Mathematical expressions describe elementary potential flows in the complex plane, from which an angle field is calculated across the rectangular domain. B) Streamlines are computed from the angle field such that the largest distance between neighboring paths does not exceed $2D_N$. C) The paths are transformed into g-code and 3D-printed, covering the area homogeneously. D) The distribution of line widths is compared between the planned toolpath (blue) and the image of the printed object (red) along a set of orthogonal "sampling" streamlines, indicating varying levels of accuracy between the response of the polymer and the planned extrusion width depending on the pattern. E) This workflow is successfully applied to a natural pattern such as the weathered wood grain of a maple log (Image credit: © Mark Windom).

© 2023 The Authors. Advanced Materials published by Wiley-VCH GmbH

15214095, 0, Downloaded from https://onlinelibrary.wiley.com/doi/10.1002/adma.202307444 by Tu Delft, Wiley Online Library on [11/01/2024]. See the Terms and Conditions (https://onlinelibrary.wiley.com/terms-and-conditions) on Wiley Online Library for rules of use; OA articles are governed by the applicable Creative Commons License

such a comparison along a representative sampling streamline for the three cases represented. The distribution of line widths for planned and printed lines in Figure 3d follows a Gaussian pattern in all three cases. The largest deviation to the expected distribution corresponds to the point source case. Due to the radial distribution of distances, the line width along each of the intersecting circles should be constant, which is not the case in the physical printed object. Looking closer at the printed lines in Figure S7 (Supporting Information), the deviation can be attributed to errors in the distinction of printed line boundaries and slight overlapping between printed lines. Depending on the fabrication sequence, if a printed line is slightly impinging onto the space of the upcoming one due to local over-extrusion, the distribution of line widths will oscillate between two values whose mean is the target extrusion value. This phenomenon dissipates without intervention but contributes largely to the larger spread of values for printed lines and could impact mechanical performance.

To replicate a more complex pattern, a principle of superposition can be used. Different base patterns can be superimposed with coefficients, as illustrated in Figure 3e, using a weathered maple log as a source image. The radius of influence on the global angle field can also be restricted simply by the element-wise product of the angle matrix with a masking matrix whose values range from 0 to 1. The impact of upper and lower bounds of line widths on the overall streamline distribution using this pattern, as well as the resulting height profile of this shape, can be seen in Figures S8–S10 (Supporting Information). A curve generation method based on phase fields [24] is compared to our streamline-based approach in Figure S12 (Supporting Information). Instead of one single relatively tortuous path with many U-turns, our approach yields multiple smoother lines. Hence, the workflow proposed here leads to 3D-printing of geometrical patterns ranging from vortices to eggbox shapes, which can easily be superimposed to capture both local and global features.

2.4. Tuning Mechanical Performance via Large-Curvature Patterns

This freedom of path generation, along with the anisotropy of LCP, opens the possibility to explore mechanical features beyond the traditional restricted fiber path of laminated materials such as high-performance continuous fiber composites. This is illustrated in **Figure 4** both in the elastic region with a buckling optimization (Figure 4a) and during fracture to deflect the propagation of a crack (Figure 4b).

In Figure 4a, the consequences of alleviating the curvature constraints on the mechanical performance are explored in the case of buckling. While we propose a simple mathematical method to generate angle fields, optimization algorithms can also be used as input to the streamline-placement workflow. We demonstrate this with an algorithm that optimizes the fiber angle distribution[6] to maximize the buckling load of 3D-printed LCP plates. In this method, fiber angle retrieval is performed by approximating the structural responses based on the optimal stiffness distribution found for a set of lamination parameters. During the optimization, a steering constraint is introduced to ensure the manufacturability of the material. Such variable stiffness laminates are typically manufactured with automated fiber placement (AFP) of continuous fiber composites. In AFP and continuous carbon-fiber 3D printing (CCF-3DP), maximum curvatures of ≈3 and 66 m^{-1}, respectively, are conservative limits to the fabrication.[6,56] At higher curvatures, defects such as wrinkling can be expected due to the intrinsic stiffness of the fibers. In contrast, the maximum curvature that can be explored here is only limited by nozzle diameter, in the range of 1000 to 2500 m^{-1}. To explore the relationship between curvature and buckling load, four different symmetric and balanced layups were generated by the optimization algorithm with allowed curvature constraints spanning from 0.1 to 1000 m^{-1} for 112 × 86 mm samples. To focus on the effect of the curvature of the printed paths, the range of line width is restricted such that more than 70% of the aggregated length of deposited lines have widths between 0.30 and 0.45 mm, close to the nozzle diameter dimension of 0.4 mm. As shown in Figure S13 (Supporting Information), the average Young's modulus across this line width range is 21.4 GPa, with a standard deviation of 1.97 GPa. The angle field and subsequent print paths for a given layer are shown in Figure 4a with a coarse line width for visualization purposes. Print paths for other curvatures can be seen in Figure S14c (Supporting Information). The distribution is unidirectional with a 45° angle at 0.1 m^{-1} curvature constraint, but at 100 m^{-1}, two distinct zones start to materialize. Edges, where stiffness is maximized, appear when the load can be redistributed to the nearby simply-supported fixture clamps in the 0° direction, and an oblique central zone emerges to resist buckling. At 1000 m^{-1}, a central transition zone is also clearly observed where the curvature changes abruptly. Samples were tested in compression until failure with the boundary conditions illustrated in Figure S14a (Supporting Information). The quantitative difference between numerical and experimental values was as expected and may be attributed in part to the simplifying assumption chosen in the optimization algorithm stating that the LCP is an orthotropic material with a constant stiffness, despite a narrow range of line width being used. Further, buckling is strongly affected by experimental perturbations which can be either induced by imperfect clamping or manufacturing defects that are common in 3D-printing. The deviation to the trend at 1000 m^{-1} can be explained by the more abrupt changes in angles resulting in a lack of continuity between print lines in this zone (Figure S14c, Supporting Information), as opposed to the smoother pattern at 100 m^{-1}. Despite these discrepancies, similar behavior is observed for both experiment and theoretical values, with an improvement between 0.1 and 100 m^{-1} of 43% numerically and 40% experimentally. This concludes that the proposed workflow can explore new pathways in mechanical design, which were previously restricted by manufacturing constraints. Furthermore, since stiffness variation of the material due to line width was minimized, the trend may also be applied to anisotropic printable materials such as fiber-filled polymers with a narrower range of property variation.

Having studied how the design space of an optimization framework can be extended via manufactured gradients of curvature and stiffness, we now explore the possibility of using the patterns described in Figure 3 to influence crack propagation. For this purpose, in Figure 4b the failure behavior of two-layered single-edge notch tension (SENT) samples is studied. A unidirectional sample perpendicular to the loading direction was

© 2023 The Authors. Advanced Materials published by Wiley-VCH GmbH

15214095, 0, Downloaded from https://onlinelibrary.wiley.com/doi/10.1002/adma.202307444 by Tu Delft, Wiley Online Library on [11/01/2024]. See the Terms and Conditions (https://onlinelibrary.wiley.com/terms-and-conditions) on Wiley Online Library for rules of use; OA articles are governed by the applicable Creative Commons License

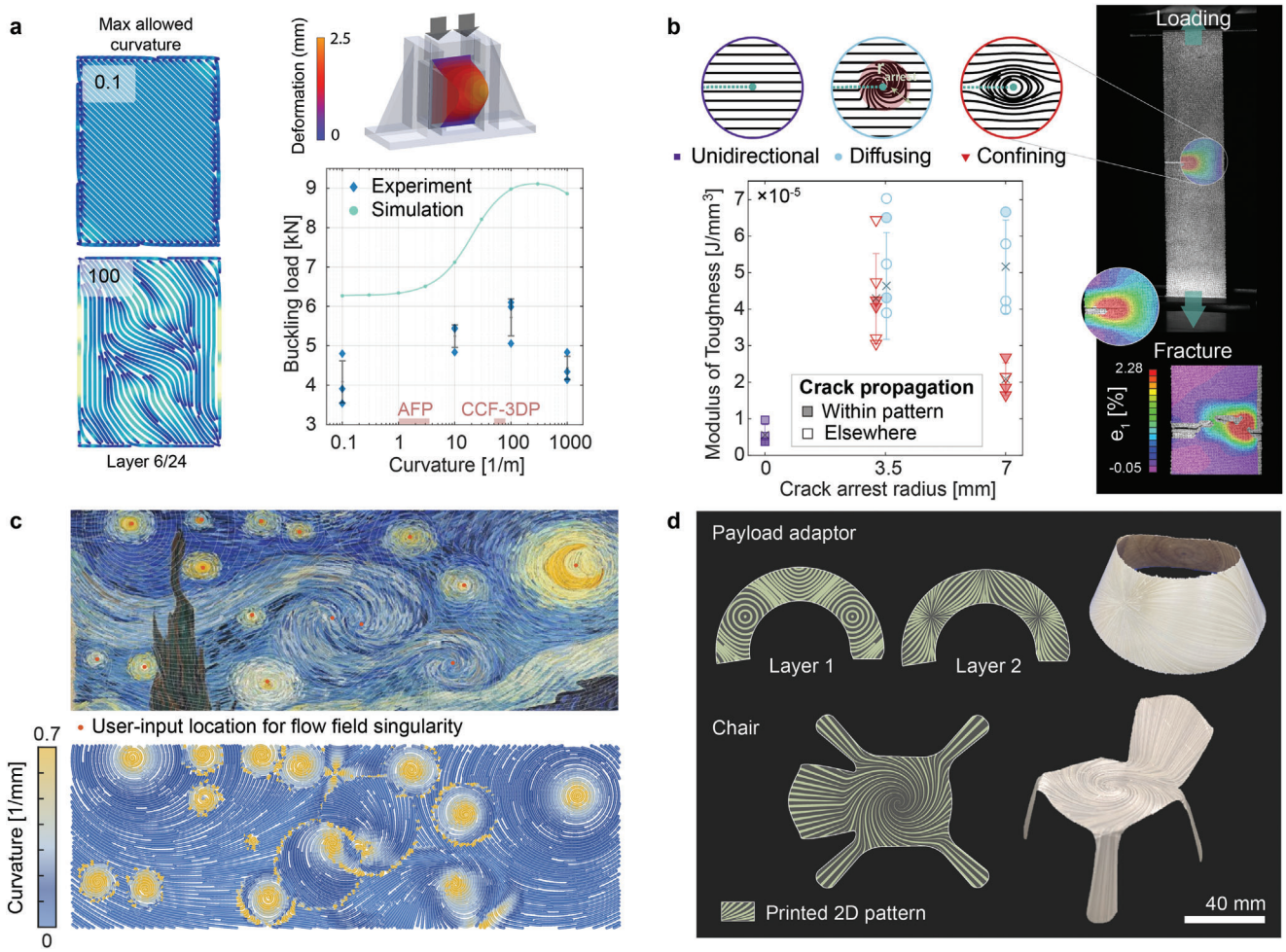

Figure 4. Patterns can be utilized to enhance mechanical properties. A) Reducing the curvature constraint in a laminate optimization algorithm[6] leads to an increase in buckling load. B) Microstructures that are locally applied to a laminate can enhance the resistance to crack propagation along a cut edge. Error bars represent the standard deviation of the data. The generated shapes can also be applied to manufacture seldom-seen patterns in solid mechanics such as turbulences, such as C) where a detail of the sky of the oil painting The Starry Night[55] by van Gogh is reproduced with vortices using the potential flow field method described in Figure 3e. 2023 Digital image, The Museum of Modern Art, New York/Scala, Florence D) The generated shapes can also open new design possibilities for functional objects such as a payload adaptor fitting for a launcher, or a chair.

taken as a benchmark. The highly-aligned microstructure of 3D-printed LCP inevitably entails a low transverse strength. Unidirectional tensile strength in the transverse direction and shear strength have been reported as 27 and 26 MPa respectively.[10] Correspondingly, the amount of energy needed to propagate the crack along the printed line direction is very low, analogous to the weak fiber interface in wood. This kind of anisotropic biomaterial adapts and grows to attenuate stress concentrations in the transverse direction.[57] In a similar approach aiming to shield sensitive zones, two different configurations were explored to resist crack propagation: a spiraling pattern, which is hypothesized to diffuse the crack course away from the notch zone, called diffusing, and a wood knot pattern, called confining as it could potentially confine the crack within the notch zone. Shown in Figure 4b, for each configuration, the radius of the crack arrest feature r_{arrest} was chosen as 3.5 or 7 mm to compare the toughness to the feature size. Compared to baseline, the modulus of toughness of samples with the smallest r_{arrest} is 7.7 times higher for the confining pattern on average, and 9.3 times higher for the diffusing pattern. From the strain fields obtained with digital image correlation (DIC), we found that none of the specimens display straight crack propagation. Due to the high toughness developed locally, the crack did not propagate from the notch where the highest stress concentration should be located. Instead, the crack was initiated at much higher loads either at another location inside the patterned zone or at a location away from the notch. The inset strain field shown in Figure 4b illustrates a propagation within the crack-arrest zone, for one of the confining samples with r_{arrest} = 3.5 mm, immediately after failure. Even though the notch is present at the center of the specimen before failure, the propagating crack avoids the center region and bridges to the opposite edge. The fact that failure takes place at another location than at the notch for 15 specimens out of 23 indicates that the proposed method may be highly successful at shielding sensitive locations, at no added mass cost.

© 2023 The Authors. Advanced Materials published by Wiley-VCH GmbH

15214095, 0, Downloaded from https://onlinelibrary.wiley.com/doi/10.1002/adma.202307444 by Tu Delft, Wiley Online Library on [11/01/2024]. See the Terms and Conditions (https://onlinelibrary.wiley.com/terms-and-conditions) on Wiley Online Library for rules of use; OA articles are governed by the applicable Creative Commons License

Alternatively, these features could be used as structural fuses to attract cracks to specific locations facilitating monitoring of predictable damage and maintenance for larger engineering systems. Both path directionality and gradient of stiffness may be independently controlled with our method, to influence deformation behavior and favor a specific failure mode. Figure S15 (Supporting Information) shows numerically how the maximum curvature of the deflecting shape of a plate subjected to pressure can be influenced by a chosen stiffness distribution[67], with for instance a more compliant and ductile material configuration along its edges.

To further illustrate the versatile nature of our approach toward the fabrication of natural materials and phenomena, we replicated an artwork well-known for its exquisite ability to capture movement through brushstrokes. In Figure 4c, the eddies in the sky of Starry Night[55] by painter Vincent van Gogh (1889) are reproduced with vortices of varying radii of influence. The corresponding evenly distributed and printable toolpaths are colored with absolute curvatures to highlight the vortex location. Despite the eddies in the painting not accurately recreating mathematical features of turbulent flow,[58] their rapid change in curvature and stroke thickness embodies the motion of turbulences in the eye of many. We find that van Gogh freely exploited a color scheme of contrasting ultramarine blues to warm yellows which can be related to the curvature of his thick impasto brushstrokes. This link between color and shape, bridging between style and content, may contribute to convey the striking combination of harmony and turmoil which has fascinated generations.[59] One could even obtain different renderings using our patterning method, with other anisotropic properties such as structural colors[60] or birefringence.[22,61] Further, integrating the concept of turbulences into solid objects opens routes for materials with new functionalities, such as the shaping of eddy currents[62] via conductive anisotropic polymers.

In Figure 4d, proof of concept functional objects that may benefit from complex patterns are presented. A truncated cone was printed in two dimensions and thermally fused at its edges, with a pattern generated from the complex velocity function $f(z) = \sin(\frac{x}{\lambda}) + i\sin(\frac{y}{\lambda})$. The geometry represents a payload attachment fitting for a space launcher, demonstrating how this method could be used to promote specific buckling modes for non-planar shapes. Next, a chair was formed by overlapping a point source onto a vortex with a diameter of influence equal to half the domain dimension. High-curvature print paths provide out-of-plane compliance at the center of the seat and straighten out gradually to distribute the load to the stiffer, unidirectional legs.

3. Conclusion

We discovered that structures can benefit from the high shaping freedom achieved with nematically aligned LCP 3D printing. The wide range of line widths that can be printed with LCP enables the modulation of mechanical behavior within a single material simply by using nozzle pressure. The changing nozzle pressure results in a transverse flow of the nematic domains causing the stiffness to vary from 3 to 40 Gpa depending on the deposited line width and nozzle diameter. These variables were used to exploit design freedom by generating evenly distributed print paths within a desired mechanical property space. Our work enables the flow-inspired design of complex microstructures using ubiquitous inputs such as biological matter, artwork, or fiber angle optimization. In particular, we found that the buckling load could be increased by 40% by alleviating the curvature constraint in a laminate optimizer. Furthermore, the generated patterns could also effectively arrest or deflect cracks in the presence of a stress concentration. The abundance of patterns that can now be manufactured expands the design space for functional, lightweight objects with gradients of stiffness and curvature, and opens research routes to reproduce and study intricate natural patterns such as turbulences, and biological microstructures such as wood or bone.

4. Experimental Section

3D-Printing: The filament used was the thermotropic random copolymer HBA: HNA with a ratio 73:27, supplied by NematX (Switzerland). G-codes were printed on a Prusa i3 MK3S+ 3D-printer, at a nozzle temperature of 330 °C and a bed temperature of 90 °C. The 3D-printer was only modified in hardware and firmware to withstand slightly higher temperatures than its specifications. The PEI bed was coated with a spray (Dimafix, Spain) to maintain good adhesion. Brass nozzles (E3D, England) used in this paper showed an L/D ratio of 1.50 for 0.25 and 0.4 mm nozzles, and L/D = 2.0 for 0.6 and 0.8 mm nozzles. Unless otherwise stated, the 0.4 mm nozzle was used.

Print speed was 60 mm s^{-1} for single lines and mechanically-tested parts. For the smaller patterns in Figure 3 of size 30 × 30 mm, print speed was reduced to 10 mm s^{-1} such that any viscoelastic response[11] of the material did not affect the effective line width variation. For UD tensile samples, a 0.05 mm layer height was used, with a print speed of 35 mm s^{-1} and a temperature of 295 °C.

Optical Microscopy: Thin strands of LCP were glued to microscopy glass slides with cyanoacrylate glue. Polishing was carried out manually on a polishing machine (Tegramin-20, Struers) with very short steps mostly in the 45°, 90° and −45° angles with respect to the longitudinal line axis to avoid peeling off the fibrillar structure until translucency was achieved (20–40 µm). An optical microscope (DM100, Leica) was used to image the cross-section with dark-field transmitted light.

SEM: A scanning electron microscope (JSM-7500F, JEOL, The Netherlands) operated with an acceleration voltage of 5 kV was used to visualize the fibrillar and core–shell structures after fracture. A 15-nm gold coating was sputtered (Quorum Q300TD, UK) on their surface prior to imaging.

Toolpath Generation—Evenly-Distributed Placement of Streamlines: Streamlines were generated in MATLAB (MathWorks, USA) from an angle field via a farthest-point seeding method inspired by Mebarki's approach.[54] In the initialization stage, a Delaunay triangulation of the edges of the rectangular design space Ω was performed. The first seeding point was the center of the largest circle circumscribed in any of the triangles inside Ω. This streamline was generated using forward Euler prediction and a trapezoidal rule correction.[63] The integration step used was 10% of an element size. The current streamline function required a rectangular grid of evenly-spaced points, however, a domain of any shape could be triangulated with the Delaunay method, which imparted robustness to the workflow in case this constraint was alleviated. This approach was illustrated in Figure S6 (Supporting Information). The parameter W_{upper} determined the maximum allowable distance between streamlines. Once the first streamline was generated, its waypoints were added to the list of edge points, and a new Delaunay triangulation was performed. While the diameter of the largest circumscribed circle was larger than W_{upper}, a new streamline was generated. A trimming step was applied directly to make sure that any two streamlines were separated by a distance larger than W_{lower}. Unless otherwise stated, its default value was $W_{lower} = W_{upper}/3.5$. This smaller bound was adapted to respect the desired mechanical boundaries or manufacturable range of

© 2023 The Authors. Advanced Materials published by Wiley-VCH GmbH

15214095, 0, Downloaded from https://onlinelibrary.wiley.com/doi/10.1002/adma.202307444 by Tu Delft, Wiley Online Library on [11/01/2024]. See the Terms and Conditions (https://onlinelibrary.wiley.com/terms-and-conditions) on Wiley Online Library for rules of use; OA articles are governed by the applicable Creative Commons License

line width as illustrated in Figure 2. The influence of W_{lower} was illustrated in Figure S9 (Supporting Information). Another parameter could be used optionally to further influence distribution of line widths, W_{seed}. As shown in Figure S8 (Supporting Information), an initial round of seed points could be spaced by a distance W_{seed} along a specified edge of the domain. This feature was useful for uniform flow fields or to steer the average distribution of line width toward the upper or lower bound. After these initial streamlines were placed, the algorithm described in Figure S6 (Supporting Information) took over to fill the remaining space.

Toolpath Generation—Line Width Calculation: Once streamlines were generated, the final distance between all of them should be computed. For each streamline S, a Delaunay triangulation was performed with all waypoints P except P_s, the set of vertices belonging to S. It was expected for each point p in P_s, two nearest neighbor points to find on either side of S. The first nearest points N_{S1} to P_s were identified with a Nearest-neighbor algorithm. The nearest neighbor algorithm was repeated without N_{S1} in order to find the second-nearest neighbors N_{S2}. The line width to be extruded at each vertex in P_s was set as half the average value of the distance to either two nearest points. This was a simplification due to the impossibility of distributing material asymmetrically on either side of the extrusion direction. These steps were repeated for each layer of the printed object.

Toolpath Generation—Post-Processing of Toolpaths: Subsequently, a Ramer–Douglas–Peucker algorithm[64,65] was applied to each streamline in order to reduce the number of way-points with a set tolerance of 0.02 mm as the maximal Euclidian distance allowed between the new line and a vertex. Three metrics were taken into account to calculate similarity: x and y coordinates, and line width. This allowed the number of points to significantly reduce despite the small iteration step. Overloading the buffer of the 3D-printer would cause inaccurate printing speed. The simplified streamlines were then ordered to minimize the distance between travel moves. The endpoint of the first streamline was connected to the closest among all extremity points of remaining streamlines until all streamlines were connected. Finally, the g-code was generated. The extrusion amount was calculated by multiplying the distance between waypoints, layer height, and line width.

Toolpath Generation—Line Width Comparison: Orthogonal sampling streamlines were computed from the vector field orthogonal to the one generating the print path. The seeding points of the N sampling streamlines were the vertices of an N-sided polygon. N was chosen to intercept between 500 and 600 printed lines. In the "point source case", orthogonal streamlines were circles, thus they were chosen with a diameter of 12, 20, and 28 mm, as 3D prints are 30 mm wide.

Image processing for 3D-printed images was performed via the following steps: first, photographs of the 3D-printed objects were taken with a Keyence VR-5000 wide-angle microscope. Next, a Photocopy filter was applied in Photoshop (Adobe, USA) to enhance the contrast between lines. In MATLAB, the image size was multiplied by four and blurred with a 2-D Gaussian smoothing kernel of a standard deviation of eight. Blurring enabled to simplify and increase the accuracy of the central location of the darker zone where two printed lines were in contact, and reduced the false positives linked to the roughness of LCP. The pixel profile along the sampling streamlines was retrieved, and peaks in the intensity values (boundaries between printed lines) were detected when they reach a prominence of 10%. Finally, the distance between peaks was computed to obtain the printed line width. For the computed line width, each theoretical polyline was checked for intersection with the orthogonal sampling streamlines. If an intersection was found, the line width of the intersecting segment was retrieved.

Once the printed and computed line widths at the intersections were found, they could be compared directly in a plot (Figure S6c, Supporting Information) for one sampling streamline, or their distribution could be compared in a histogram (Figure 3d). The height of all the bars was summed to 100% as each bar height represented the percentage of intersected points that fall under a given range of line width.

Tensile Testing—Single-Line Testing: For each print batch, 8 to 10 single lines of the same width were deposited in a bidirectional raster pattern, resulting in lines of ≈100 mm in length. To prevent edge effects, a gauge length of 20 mm was marked directly on the line at half-length. Images of this portion of the lines were captured on a wide-angle 3D scanner (VR-5000, Keyence, Japan) while still attached to the print bed. This enabled to measure width without perspective error. The images were transformed into binary masks in MATLAB, such that white pixels on the transverse axis yield the width continuously along the longitudinal axis. The average width was then calculated.

Single lines were individually glued onto paper tabs at their measured gauge-length position. The tensile tests were carried out at a rate of 2 mm min^{-1} using a 10 kN (Zwick Roell, Germany) universal testing machine equipped with a 100 N load cell (HBM, Germany). Post-processing was performed with a custom MATLAB script.

Tensile Testing—Unidirectional Tensile Testing: The unidirectional parts were tested under tension using a Z020 (Zwick, Germany) universal testing machine with a 20 kN capacity load cell. Following ISO 527-5, samples with a nominal width of 5 mm, length of 110 mm, and thickness of 2 mm were printed at 0° angle to the tensile direction, varying the line width from 0.2 to 0.6 mm with a 0.4 mm nozzle diameter. Bonded glass fiber end tabs supported the clamping region resulting in a gauge length of 65 mm. Five samples were tested per batch, at a displacement rate of 2 mm min^{-1}.

Tensile Testing—Single-Edge Notch Tension: Two-layered 3D-printed samples of size 90 × 20 mm were tested with a 10 kN (Zwick Roell, Germany) machine equipped with a 100 N load cell. The notch was created with a sharp razor with extra care to avoid any transverse force pulling apart the lines.

DIC: Digital image correlation was used to measure the local displacements of the SENT specimens. One 9 MP camera (LIMESS, Germany) with a 50 mm-focal length lens was used to acquire images at a rate of 2 Hz. Analysis was performed using Vic-2D 6 (Correlated Solutions), with a subset size and step size of 27 and 7. A speckle pattern size of 0.18 mm m was applied with a stamping roll and ink (Correlated Solutions).

Buckling—Laminate Optimization Code: Theoretical values of buckling loads in Figure 4a were computed with the algorithm of Peeters[6] for an orthotropic material similar to LCP, whose stiffness was assumed to not change with line width. The values E_{11} = 15.4 GPa, E_{22} = 2.08 GPa, G_{12} = 1.3 GPa, ν_{12} = 0.57 were used, as reported in[10] for a layer height of 0.1 mm. A frame was padded around the edges of the output angle field such that the laminate optimization described the design zone, but that enough space was left to apply vertical clamped or lateral pinned boundary conditions.

Buckling—Compression Fixture: 3D-printed laminates of 112 × 86 mm with 24 layers of a balanced, symmetric layup were subjected to compression. A modified[66] compression after impact fixture was used to introduce the top compressive load and kept the top and bottom of the plate clamped, and lateral edges simply supported with knife edges, as described in Figure S14a (Supplementary Information). Load was introduced by a 10 kN test bench (Zwick, Germany) with controlled-displacement at a rate of 2 mm min^{-1}. Buckling load was determined as the first point where the load deviated by 100 N from the linear regression determined in the elastic zone from 500 N onward.

Shaping of 3D-Objects: To fuse flat printed shapes and create a 3D object, the material could be melted again after extrusion. Kapton tape was first applied to protect the material. The hot tip (290 °C) of a soldering iron was applied briefly at the desired location and angle. The position was maintained until solidification.

Supporting Information

Supporting Information is available from the Wiley Online Library or from the author.

Acknowledgements

The authors acknowledge ESA through the support of C.H. via the Open Science Innovation Platform grant No. 4000131850. The authors also thank André R. Studart at ETH Zurich and Clemens Dransfeld at TU Delft

© 2023 The Authors. Advanced Materials published by Wiley-VCH GmbH

15214095, 0, Downloaded from https://onlinelibrary.wiley.com/doi/10.1002/adma.202307444 by Tu Delft, Wiley Online Library on [11/01/2024]. See the Terms and Conditions (https://onlinelibrary.wiley.com/terms-and-conditions) on Wiley Online Library for rules of use; OA articles are governed by the applicable Creative Commons License

for helpful discussions. The authors also appreciate the support of Derin Ulcay for adding features to Slith3r, the open-source path-generating code.

Conflict of Interest

S.G. and K.M. are co-inventors of a patent application on liquid crystal polymer 3D printing and co-founders of NematX AG.

Author Contributions

C.H., V.D., S.G., and K.M. conceived the research and designed the experiments. Software was developed by C.H., V.D., and D.P. Investigation was carried out by C.H., V.D., C.M., and S.G. K.M. supervised the research. C.H. and K.M. wrote the original draft. Writing review and editing was performed by C.H., V.D., C.M., S.G., D.P., and K.M.

Data Availability Statement

The data that support the findings of this study are available from the corresponding author upon reasonable request.

Keywords

additive manufacturing, bio-inspired materials, gradients, liquid crystal polymers, mechanical anisotropy, toughening

Received: July 26, 2023
Revised: December 6, 2023
Published online:

[1] J. Färber, H. C. Lichtenegger, A. Reiterer, S. Stanzl-Tschegg, P. Fratzl, *J. Mater. Sci.* **2001**, *36*, 5087.
[2] T. N. Sullivan, B. Wang, H. D. Espinosa, M. A. Meyers, *Mater. Today* **2017**, *20*, 377.
[3] M. Hu, A. Olsson, S. Hall, T. Seifert, *Wood Sci. Technol.* **2022**, *56*, 147.
[4] R. Weinkamer, P. Fratzl, *Mater. Sci. Eng. C* **2011**, *31*, 1164.
[5] J. F. V. Vincent, O. A. Bogatyreva, N. R. Bogatyrev, A. Bowyer, A.-K. Pahl, *J. R. Soc. Interface* **2006**, *3*, 471.
[6] D. M. J. Peeters, G. G. Lozano, M. M. Abdalla, *Comput. Struct.* **2018**, *196*, 94.
[7] G. Zucco, M. Rouhi, V. Oliveri, E. Cosentino, R. M. O'higgins, P. M. Weaver, *AIAA J.* **2021**, *59*, 5117.
[8] J. Chen, X. Liu, Y. Tian, W. Zhu, C. Yan, Y. Shi, L. B. Kong, H. J. Qi, K. Zhou, *Adv. Mater.* **2022**, *34*, 2102877.
[9] H. Zhang, J. Chen, D. Yang, *Addit. Manuf.* **2021**, *38*, 101775.
[10] S. Gantenbein, K. Masania, W. Woigk, J. P. W. Sesseg, T. A. Tervoort, A. R. Studart, *Nature* **2018**, *561*, 226.
[11] S. Gantenbein, C. Mascolo, C. Houriet, R. Zboray, A. Neels, K. Masania, A. R. Studart, *Adv. Funct. Mater.* **2021**, *31*, 2104574.
[12] S. Hornus, T. Kuipers, O. Devillers, M. Teillaud, J. Martínez, M. Glisse, S. Lazard, S. Lefebvre, *ACM Trans. Graphics* **2020**, *39*, 131:1.
[13] T. Kuipers, E. L. Doubrovski, J. Wu, C. C. L. Wang, *Comput. Aided Des.* **2020**, *128*, 102907.
[14] A. Moetazedian, A. S. Budisuharto, V. V. Silberschmidt, A. Gleadall, *Addit. Manuf.* **2021**, *37*, 101576.
[15] J. Yan, E. Demirci, A. Ganesan, A. Gleadall, *Addit. Manuf.* **2022**, *49*, 102496.
[16] J. Yan, E. Demirci, A. Gleadall, *Rapid Prototyping J.* **2023**, https://doi.org/10.1108/RPJ-09-2022-0315.
[17] E. Bertevas, J. Férec, B. C. Khoo, G. Ausias, N. Phan-Thien, *Phys. Fluids* **2018**, *30*, 103103.
[18] B. Šeta, M. Tusher Mollah, V. Kumar, D. Kumar Pokkalla, S. Kim, A. Arabi Hassen, J. Spangenberg, Proc. 33rd Ann. Int. Solid Freeform Fabrication Symp. – An Additive Manufacturing Conf., Texas, USA, November **2022**.
[19] A. Bedel, Y. Coudert-Osmont, J. Martínez, R. I. Nishat, S. Whitesides, S. Lefebvre, *Comput. Graphics Forum* **2022**, *41*, 473.
[20] N. Boddeti, Y. Tang, K. Maute, D. W. Rosen, M. L. Dunn, *Sci. Rep.* **2020**, *10*, 16507.
[21] X. Chen, G. Fang, W. Liao, C. C. L. Wang, *Addit. Manuf.* **2022**, *49*, 102470.
[22] X. Chermain, C. Zanni, J. Martínez, P.-A. Hugron, S. Lefebvre, *ACM Trans. Graphics* **2023**, *42*, 1.
[23] T. Tricard, J. Etienne, C. Zanni, S. Lefebvre, *Proc. – SCF 2021 ACM Symp. Comput. Fabr.* **2021**, *7*, 1.
[24] N. Ichihara, M. Ueda, *Compos. Part B Eng.* **2022**, *232*, 109626.
[25] N. Ichihara, M. Ueda, *Compos. Part B Eng.* **2023**, *253*, 110572.
[26] V. Murugan, G. Alaimo, F. Auricchio, S. Marconi, *Addit. Manuf.* **2022**, *59*, 103064.
[27] X. J. Niu, T. Yang, Y. Du, Z. Q. Xue, *Arch. Appl. Mech.* **2016**, *86*, 1551.
[28] T. Shafighfard, T. A. Cender, E. Demir, *Addit. Manuf.* **2021**, *37*, 101728.
[29] A. V. Malakhov, X. Tian, Z. Zheng, T. P. Plugatar, Y. Huang, N. A. Tatus', D. Li, *Compos. Struct.* **2022**, *299*, 116091.
[30] B. Seshadri, I. Hischier, K. Masania, A. Schlueter, *Adv. Mater. Technol.* **2023**, *8*, 2300403.
[31] L. L. Chapoy, B. R. Marcher, K. H. Rasmussen, *Liq. Cryst.* **1988**, *3*, 1611.
[32] A. Romo-Uribe, A. H. Windle, *Proc. R. Soc. A* **1999**, *455*, 1175.
[33] D. E. Turek, G. P. Simon, *Polymer* **1993**, *34*, 2763.
[34] A. Reyes-Mayer, B. Alvarado-Tenorio, A. Romo-Uribe, R. Benavente, M. Jaffe, A. Molina-Ocampo, *Polym. Adv. Technol.* **2016**, *27*, 748.
[35] W. A. Côté, R. B. Hanna, *Wood Fiber Sci.* **1983**, *2*, 135.
[36] M.-C. Maaß, S. Saleh, H. Militz, C. A. Volkert, *Adv. Mater.* **2020**, *32*, 1907693.
[37] J. C. Gibbings, *Dimensional Analysis*, Springer, London, **2011**.
[38] E. Peuvrel, P. Navard, *Macromolecules* **1991**, *24*, 5683.
[39] A. M. Donald, C. Viney, A. H. Windle, *Polymer* **1983**, *24*, 155.
[40] N. J. Alderman, M. R. Mackley, *Faraday Discuss. Chem. Soc.* **1985**, *79*, 149.
[41] J. Ding, J. Feng, Y. Yang, *Polym. Bull.* **1996**, *36*, 773.
[42] J. Vermant, P. Moldenaers, J. Mewis, S. J. Picken, *J. Rheol.* **1994**, *38*, 1571.
[43] G. Marrucci, F. Greco, *Advances in Chemical Physics*, Wiley, Hoboken, New Jersey **1993**, pp. 331–404
[44] D. Grecov, A. D. Rey, *J. Non-Newtonian Fluid Mech.* **2006**, *139*, 197.
[45] J. Wang, M. M. Labes, *Macromolecules* **1992**, *25*, 5790.
[46] C. J. G. Plummer, B. Zülle, A. Demarmels, H.-H. Kausch, *J. Appl. Polym. Sci.* **1993**, *48*, 751.
[47] N. M. Larson, J. Mueller, A. Chortos, Z. S. Davidson, D. R. Clarke, J. A. Lewis, *Nature* **2023**, *613*, 682.
[48] J. R. Raney, B. G. Compton, J. Mueller, T. J. Ober, K. Shea, J. A. Lewis, *Proc. Natl. Acad. Sci. USA.* **2018**, *115*, 1198.
[49] D. Kokkinis, F. Bouville, A. R. Studart, *Adv. Mater.* **2018**, *30*, 1705808.
[50] P. A. G. S. Giachini, S. S. Gupta, W. Wang, D. Wood, M. Yunusa, E. Baharlou, M. Sitti, A. Menges, *Sci. Adv.* **2020**, *6*, 0929.
[51] C. Waly, S. Petersmann, F. Arbeiter, *Adv. Eng. Mater.* **2023**, *25*, 2101703.
[52] H. Chanson, *Applied Hydrodynamics – An Introduction to Ideal and Real Fluid Flows*, CRC Press, Taylor & Francis Group, Boca Raton, **2009**.

© 2023 The Authors. Advanced Materials published by Wiley-VCH GmbH

15214095, 0, Downloaded from https://onlinelibrary.wiley.com/doi/10.1002/adma.202307444 by Tu Delft, Wiley Online Library on [11/01/2024]. See the Terms and Conditions (https://onlinelibrary.wiley.com/terms-and-conditions) on Wiley Online Library for rules of use; OA articles are governed by the applicable Creative Commons License

[53] H. Chanson, in, *Appl. Hydrodyn. an Introd.*, Taylor & Francis, Boca Raton, **2014**, p. 146.
[54] A. Mebarki, P. Alliez, O. Devillers, *Proc. IEEE Vis.*, IEEE, New York City **2005**.
[55] V. van Gogh, "The Starry Night," Oil on canvas, 29×36 ¼ (73,7×92,1 cm). Acquired through the Lillie P. Bliss Bequest. Acc.n.: 472.1941, **1889**.
[56] M. Iragi, C. Pascual-González, A. Esnaola, U. Morales, J. Aurrekoetxea, C. S. Lopes, L. Aretxabaleta, *Addit. Manuf.* **2023**, *63*, 103418.
[57] C. Mattheck, *Design in Nature : Learning from Trees*, Springer, Berlin, **1998**.
[58] W. H. Finlay, *Turbul. Mixing Nonreact. React. Flows, Proc. Proj. Squid Workshop* **2020**, *21*, 34.
[59] C. Breunesse, A. Bluhm, *J. Mus. Educ.* **2001**, *26*, 10.
[60] B. B. Patel, D. J. Walsh, D. H. Kim, J. Kwok, B. Lee, D. Guironnet, Y. Diao, *Sci. Adv.* **2020**, *6*, aaz7202.
[61] K. Fukuhara, S. Nagano, M. Hara, T. Seki, *Nat. Commun.* **2014**, *5*, 3320.
[62] M. A. Machado, L. S. Rosado, T. G. Santos, *J. Nondestr. Eval.* **2022**, *41*, 50.
[63] D. Hanselman, "Improved 2-D Streamlines", **2023**, https://www.mathworks.com/matlabcentral/fileexchange/38860-improved-2-d-streamlines, **2012**, (accessed: January 2023).
[64] D. H. Douglas, T. K. Peucker, *Can. Cartogr.* **1973**, *10*, 112.
[65] "Line Simplification," can be found under, https://www.mathworks.com/matlabcentral/fileexchange/21132-line-simplification, **2010**.
[66] M. Linke, F. Flügge, A. J. Olivares-Ferrer, *J. Compos. Sci.* **2020**, *4*, 126.
[67] S. Setoodeh, M. M. Abdalla, Z. Gürdal, *Compos. Part B Eng.* **2006**, *37*, 301.

© 2023 The Authors. Advanced Materials published by Wiley-VCH GmbH

15214095, 0, Downloaded from https://onlinelibrary.wiley.com/doi/10.1002/adma.202307444 by Tu Delft, Wiley Online Library on [11/01/2024]. See the Terms and Conditions (https://onlinelibrary.wiley.com/terms-and-conditions) on Wiley Online Library for rules of use; OA articles are governed by the applicable Creative Commons License